

# Diffusion and surface charge studies of waste cow dung derived highly porous carbon as a facile electrode for solid-state supercapacitors

Prashant Dubey<sup>a,1</sup>, Vishal Shrivastav<sup>b,1</sup>, Bhavana Gupta<sup>b</sup>, Marcin Holdyński<sup>b</sup>, Wojciech Nogala<sup>b</sup>, Shashank Sundriyal<sup>a,b,\*</sup>

<sup>a</sup> Advanced Carbon Products and Metrology Department, CSIR-National Physical Laboratory (CSIR-NPL), New Delhi 110012, India

<sup>b</sup> Institute of Physical Chemistry, Polish Academy of Sciences, Kasprzaka 44/52, 01-224 Warsaw, Poland

## ARTICLE INFO

### Keywords:

Biowaste  
Activated carbon  
Supercapacitor  
Cow dung  
Surface charge contribution

## ABSTRACT

Carbon-based materials generated from biowaste have recently attracted interest due to their exceptional surface and conductive properties. Cow dung derived porous carbon (CDPC) with a 3D structure and linked pores is synthesized in this study, making it an alternative electrode for supercapacitors (SC). Herein, we studied the diffusion and surface charge contribution and their relationship with the scan rate. Diffusion charge contribution is more prevalent at lower scan rates. Furthermore, a large fraction of surface charge contribution of 69.2 % at a high scan rate of 100 mV/s indicates rapid electrochemical kinetics and hence high-rate performance even at higher current densities. In addition, utilizing a 1 M H<sub>2</sub>SO<sub>4</sub> electrolyte, the CDPC electrode has attained a high specific capacitance value of 210 F/g at 0.5 A/g. Furthermore, symmetrical solid-state SC device displayed high energy density of 36 Wh/kg at good power density of 800 W/kg along with remarkable cyclic stability of 92.6 % after 10,000 charge-discharge cycles. Hence, these findings demonstrate that investigating surface and diffusion charge contributions opens up new avenues for tuning the supercapacitor performance.

## 1. Introduction

One of the most hotly debated subjects in contemporary research is the desire for innovative and alternative energy storage systems. As a result, researchers are paying close attention to supercapacitors, which have a high specific capacitance (Cs), high cyclic stability, and moderate energy but high power density [1,2]. As a result, various researchers have been working to enhance the energy density of SC along with extended cyclic stability. The adoption of appropriate high-performance electrode materials is the most important technique to enhance the energy density of SCs [3–5]. In reality, every carbon and its associated materials such as activated carbon (AC), carbon nanotubes, and graphene work on the EDL phenomena and are therefore employed as active electrodes in EDLC [6–8].

In comparison to commercial activated carbon analogues, AC with a high SSA, and superior conductivity is must for SCs. As a result, biowaste-derived carbons are popular electrodes for SCs due to its easy production, good conductivity, and high SSA etc. In a study, Zhang et al. used *Helianthus annuus* to create three-dimension porous carbon sponge

like nanostructure and delivered a high Cs of 403.6 F/g at 0.5 A/g in a 6 M KOH electrolyte [9]. In another study, Yu et al. synthesized ground cherry (*Physalis philadelphica* Lamarck) derived 3D carbon nanosheets which attained a high Cs of 350 F/g at 0.1 A/g in 6 M KOH electrolyte [10]. Obtaining AC from biowaste can be accomplished in one or more processes. This might involve the biowaste's cellulose or lignin degradation, which is generally followed by a series of activation stages [4,11]. The activation stages are critical for generating porosity and organic groups within the framework of carbon, both of which are important criteria for high EDLC and pseudocapacitive performance which in turn improves the overall electrochemical performance [12–14]. The degree of carbon graphitization and inherent availability of heteroatoms are two more factors that can increase capacitance that can be tuned by the usage of activating agents [15–17]. However, these activation agents might raise the total cost and add extra stages to the synthesis. As a result, choosing the right biomass resource with inherent heteroatoms, functional groups, and porosity is critical for SCs [10,18–20].

We concentrated our efforts on determining the charge contribution

\* Corresponding author at: Institute of Physical Chemistry, Polish Academy of Sciences, Kasprzaka 44/52, 01-224 Warsaw, Poland.

E-mail address: [ssundriyal@ichf.edu.pl](mailto:ssundriyal@ichf.edu.pl) (S. Sundriyal).

<sup>1</sup> Both authors contributed equally.

parameters for CDPC, which are key criteria for rapid charging and discharging. We have also done extensive research on the electrolyte's behaviour during charge storage and optimization. Cow dung has plethora of applications in past such as cooking fuel, for making houses in rural areas etc. However, with the introduction modern technology, the application of cow dung has been declined greatly. We used cow dung to make extremely porous 3D framework carbon with interconnected pores because of easy availability, low cost, and diverse properties. We employed the hydrothermal pre-carbonization approach, which allows the creation of adequate porous morphology, that is considerably more feasible than typical pyrolysis carbonization. The novelty of this work lies in the study of surface and diffusion charge contribution investigation which tells us how the charge contribution behave with respect to scan rate. To the best of our knowledge, surface and diffusion charge contribution investigation of cow dung based activated carbon has not been reported for supercapacitor application so far. Notably, CDPC shows highest level of porosity when activated at 800 °C which in turn helps to achieve the remarkable electrochemical performance of SCs.

## 2. Experimental

### 2.1. Materials

The cow dung was procured from the local dairy farm, India. *N*-methyl-2-pyrrolidone (NMP) was purchased from Sigma Aldrich. The following chemicals were bought from Merck, India: ethanol, sulphuric acid (H<sub>2</sub>SO<sub>4</sub>), and hydrochloric acid (HCl). Himedia in India provides the pellets of potassium hydroxide and polyvinylidene fluoride (PVDF).

### 2.2. Synthesis of cow dung derived porous carbon (CDPC)

The collected cow dung was cleaned 4–5 times with ethanol and deionized water before being dried in vacuum oven at 100 °C for 24 h and pulverised into powder form. The as obtained powder is then kept in autoclave (Teflon-lined) with 1 M H<sub>2</sub>SO<sub>4</sub> and heated at 180 °C for 24 h for pre-carbonization. The product is next rinsed 5–6 times to remove any acidic content and further dried in oven. For chemical activation, the cleaned pre-carbonized product is blended in a 1:2 ratio (by weight) with KOH and then heated at 800 °C for 3 h after reaching this temperature at a ramp rate of 5 °C/min. The resulting product was agitated overnight in dilute HCl to eliminate any remaining potassium residues and finally dried to produce the desired CDPC product.

### 2.3. Characterization

A Renishaw (Invia) system with a 532 nm laser source was used to record Raman spectra analysis. A Quantachrome AsiQwin instrument was used to record the N<sub>2</sub> adsorption-desorption isotherms for the samples. Brunauere-Emmette-Teller approach was used to evaluate specific surface area of the samples. Further, pore size distribution was assessed via Barrett-Joyner-Halenda Model using adsorption branch of isotherms. X-ray diffractometer of model Bruker, D8 Advance, CuK source 1.54 Å was used to record XRD patterns. FESEM (Hitachi SU8010; applied voltage: 5–7 kV) was used to do the elemental mapping, Energy-dispersive X-ray spectroscopy (EDS), and the morphological analysis of the samples. X-ray photoelectron spectroscopy (XPS) measurements were performed using a Microlab 350 (Thermo Electron) spectrometer, with Al-Kα non-monochromated radiation (1486.6 eV; 300 W) as the excitation source and a lateral resolution of 0.2 mm<sup>2</sup>. The pressure during analysis was 5.0 × 10<sup>−9</sup> mbar. Survey spectra and high resolution spectra were recorded using 100 and 40 eV pass energy, respectively. A Shirley background subtraction was applied to obtain the XPS signal intensity. The peaks were fitted using an asymmetric Gaussian/Lorentzian mixed function.

### 2.4. Electrochemical measurements

A VMP Biologic electrochemical workstation was used to measure the electrochemical parameters of CDPC electrodes using cyclic voltammetry (CV), galvanostatic charge-discharge (GCD), and electrochemical impedance spectroscopy (EIS) methods. To begin, the CDPC active electrode was made by producing a homogeneous slurry of CDPC and PVDF in a 9:1 ratio using NMP solvent. The produced slurry was evenly deposited over graphene foil in a 1 × 1 cm<sup>2</sup> area with an active loading of 1 mg/cm<sup>2</sup> and kept for drying for 10 h. The assessment of the CDPC electrode is initially tested in a 3-electrode cell with platinum wire, Ag/AgCl, and CDPC serving as the counter, reference, and working electrodes, respectively. The electrochemical parameters and surface & diffusion contributions of CDPC electrodes are performed in a 3-electrode setup using 1 M H<sub>2</sub>SO<sub>4</sub> electrolyte. Additionally, a symmetrical all-solid-state supercapacitor was built using CDPC electrodes with equivalent mass loading. The two CDPC electrodes were sandwiched with PVA-1 M H<sub>2</sub>SO<sub>4</sub> gel, and paraffin film was used to seal the device and provide support. The solid-state supercapacitor device CDPC//CDPC was evaluated in a two-electrode electrochemical cell configuration to determine its power density, energy density, and cyclic stability.

### 2.5. Equations for electrochemical calculations

From CV and GCD curves, the corresponding specific capacitance was determined using the equations given below [21]:

$$C = \frac{\int IdV}{m v \Delta V} \quad (1)$$

$$C = \frac{I \Delta t}{m \Delta V} \quad (2)$$

where  $C$  is the specific capacitance (F/g),  $I$  represent the applied current (mA),  $\Delta V$  represents the potential difference (V),  $m$  is the active material mass (mg),  $v$  is scan rate, and  $\Delta t$  represents discharge time (s).

The energy density (Wh/kg) for the two-electrode system was determined using the equation:

$$E = CV^2/7.2 \quad (3)$$

and the power density (W/kg) was evaluated using the equation:

$$P = \frac{3600E}{t} \quad (4)$$

## 3. Results and discussion

### 3.1. Material characterization of CDPC material

Cow dung is used to create a 3D structure with linked pores, thanks to its high carbon content and heteroatoms, as well as its widespread availability in society. These intrinsic heteroatoms allow for the creation of additional micro and mesopores, increasing the porosity of manufactured CDPC material. The porosity of CDPC is determined by two critical steps: hydrothermal pre-carbonization at 180 °C and KOH chemical activation at 800 °C in an inert environment [22]. This approach is useful for producing enough micro- and mesopores, as well as a high SSA and strong conductivity, that are the essential requirements for selecting a supercapacitor electrode.

Using several structural characterization methods, the successful production of the CDPC sample is validated. To begin, an XRD analysis of a CDPC sample is done to detect the production of graphitic carbon at 800 °C. The XRD pattern of a CDPC sample are shown in Fig. 1a, and the reported peak locations are well-matched with earlier literature. The presence of turbostratic carbon with poor crystallinity is indicated by peaks in the 2 $\theta$  range of 23° (002) and 42° (100) in the CDPC sample. The major key to customizing the surface functional groups of activated

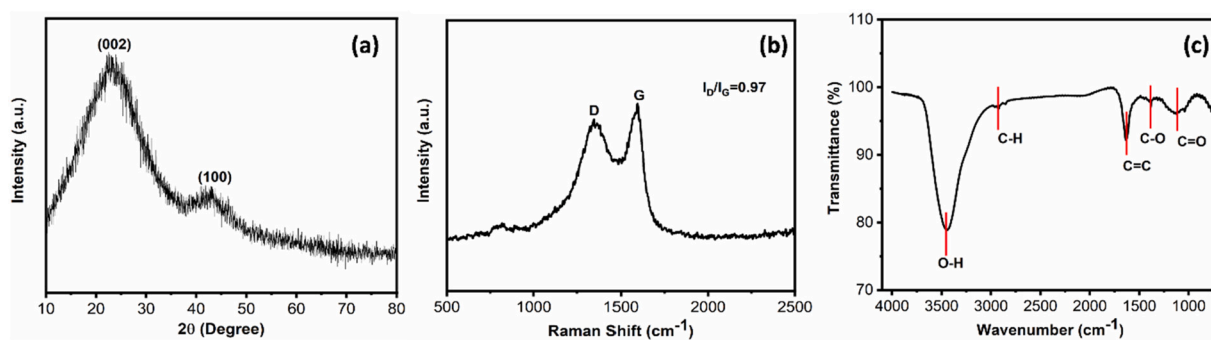


Fig. 1. (a) XRD; (b) Raman, and (c) FTIR spectrum of CDPC sample.

carbon surface textures is the hydrothermal carbonization and the activation route [23].

The vibrational modes of the molecules in the CDPC sample are investigated using a Raman spectrometer. It is the most potent analytical methods for determining the degree of functionalization in CDPC materials, as well as all carbon-based compounds. To begin, a Raman spectra was recorded in the wave-number range of 500 to 2500  $\text{cm}^{-1}$  using an excitation wavelength of 514 nm. The Raman spectra for the CDPC sample are shown in Fig. 1b, with the D and G bands situated at 1342 and 1586  $\text{cm}^{-1}$ , respectively. In CDPC material, these peaks demonstrate the presence of graphitic and disordered carbon. The G band in the CDPC sample is more intense than the D band, showing that the as-synthesized 3D structure is partially graphitized [24,25].

Furthermore, the lower  $I_D/I_G$  ratio of the CDPC framework verifies its partly graphitic structure and greater interconnectivity, ensuring that the CDPC 3D framework-based electrode has a higher conductivity.

As a result, FTIR characterization within the range of 500–4000  $\text{cm}^{-1}$  is used to investigate the surface functionalities of CDPC material. The FTIR spectrum of the CDPC sample are shown in Fig. 1c, confirming the existence of oxygen and hydroxyl groups on the surface of the material. The band at 3460  $\text{cm}^{-1}$  corresponds to –OH stretching vibrations. The aliphatic vibrations of C–H bonds is shown by small bands at 2919  $\text{cm}^{-1}$ . Furthermore, the strong peaks centered at 1635, and 1382  $\text{cm}^{-1}$  belongs to C=C and C–O stretching, respectively [26,27]. Furthermore, the C=O stretching vibration is mostly seen around 1138  $\text{cm}^{-1}$  [28].

The chemical species and surface functionalities associated to the

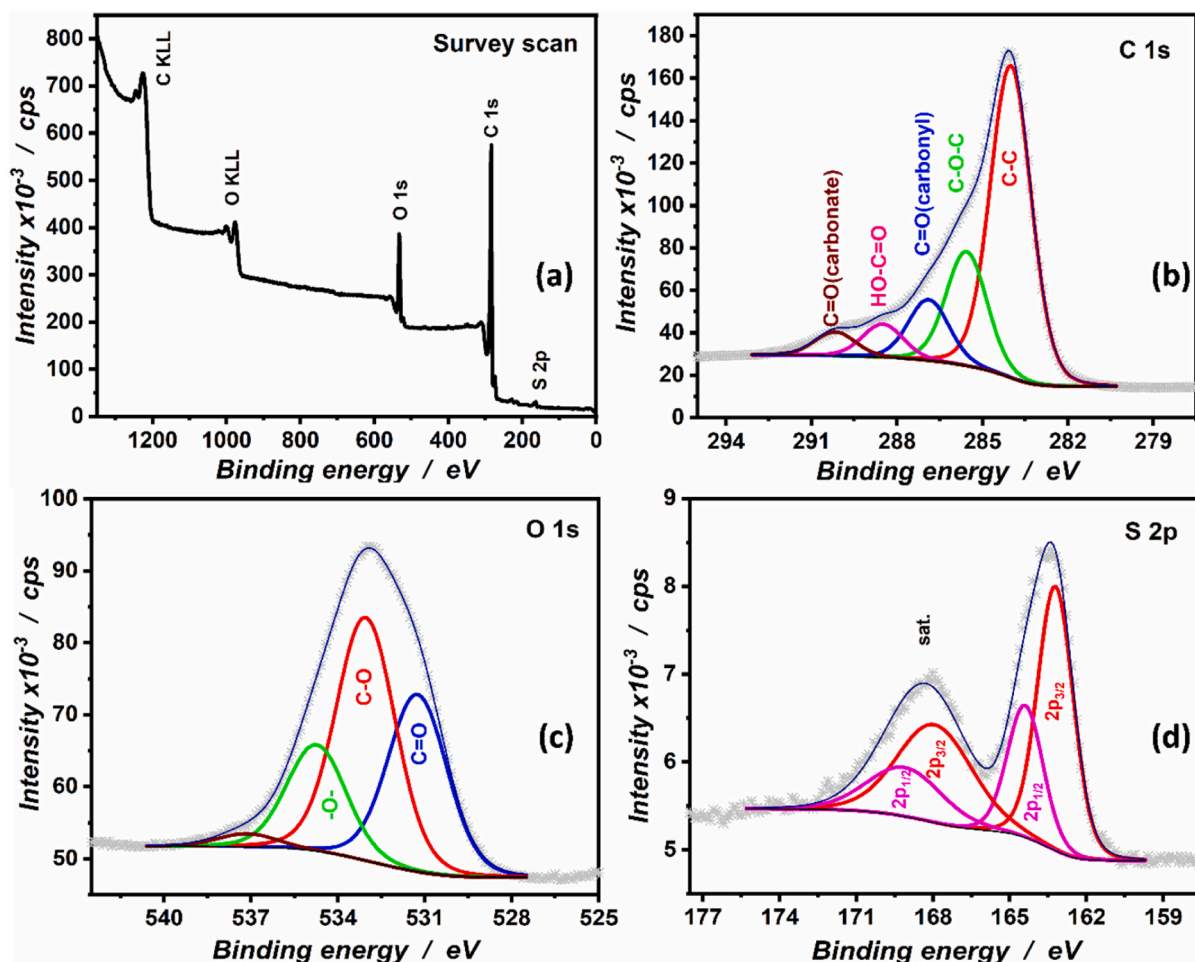


Fig. 2. XPS analysis of CDPC; (a) survey scan; (b) C 1s; (c) O 1s; and (d) S 2p

CDPC are revealed by XPS analysis, as depicted in Fig. 2a. The presence of carbon, oxygen and sulphur in the sample is demonstrated by the distinct peak at 284.8, 534.1 eV, and 163.8 eV which correspond to C 1s, O 1s, and S 2p respectively. The formation of highly pure carbonaceous material is indicated by the high intensity of the carbon peak. Fig. 2b shows the deconvoluted C 1s peaks revealing the bonding of carbon with other element. Peak located at a binding energy of 284.0 indicates the presence of C—C bonding and the peak at 285.6 eV associated with alcohol/ether group (C—O—C/C—OH) [14]. Peaks at 286.9 eV and 288.5 eV are attributed to the carbonyl (C=O) group and the carboxyl (O=C—OH) functional group, respectively. The deconvoluted O 1s spectra are shown in Fig. 2c in a similar manner. The peak at 531.2 eV indicate the presence of carbonyl (C=O), and the peak at 533.0 eV corresponds to the C—O bonding. In addition, deconvoluted spectra of S 2p is illustrated in Fig. 2d revealing the presence of S 2p<sub>1/2</sub>, and S 2p<sub>3/2</sub> bonding. The presence of oxygen and sulphur is thought to increase the electrode's wettability, facilitating an effective passage for electrolyte ions into the porous structure of electrode and increasing the electrode's capacity for charge storage.

The BET measurements are used to figure out the SSA and pore size properties of the CDPC sample. Fig. 3a depicts the N<sub>2</sub> adsorption-desorption isotherms of the CDPC sample that shows type IV behaviour (mesoporous). For the CDPC sample, the SSA and highest pore volume were 1017 m<sup>2</sup>/g and 0.503 cm<sup>3</sup>/g, respectively. The existence of thin cylindrical pores in the material is also indicated by a modest open isotherms. Further the pore size arrangement was analyzed via BJH plot (Fig. 3b). The mean pore size measured for the CDPC sample, according to BJH, is 5.4 nm. One thing to keep in mind is that chemical activation aids in the creation of mesopores within the carbon 3D framework structure formed from cow dung. The electrochemical performance of the material is highly dependent on the pore size of the material. Mesopores helps in reducing ions conducting and diffusion pathways and hence enhancing the energy storage capability of the material [29,30]. The porosity of CDPC allows the ions to access the pores, which helps to improve the overall electrochemical characteristics [31].

Aside from structural characterization, the material's surface morphology is an important characteristic in supercapacitors since a good morphology can help with the interactions of electrode and electrolyte. The carbonization and activation phases, which eliminate cellulose and lignin and generate holes in the framework, resulted in the formation of this 3D framework. The formation of a 3D interconnected porous morphology was confirmed by FESEM inspection of the as-synthesized CDPC sample (Fig. 4(a–b)). This design is helpful in supercapacitors because it allows for easy access, storage, and rapid transit of electrolyte ions. During electrochemical testing, the large pores (0.3–1 µm) can act as ion-buffering reservoirs. Furthermore, for a 3D structure, thinner CDPC sheets are linked to greater activation temperatures. The

hydrothermal pre-carbonization procedure in 1 M H<sub>2</sub>SO<sub>4</sub> solvent and the post activation process with KOH is the primary explanation for the formation of 3D framework structure in CDPC sample. To begin, majority of lignin and semi-cellulose are transformed into organics using 1 M H<sub>2</sub>SO<sub>4</sub> solvent during hydrothermal pre-carbonization at 180 °C, which reduces cellulose crystallinity and increases the porosity of bio-wastes. The FESEM of the pre-carbonized carbon is given in the Fig. 4a–b. The images shows the absence of porous framework after the pre-carbonization step.

A high temperature (800 °C) activation process is used to carbonize the crystalline cellulose and turn the cow dung into a porous carbon 3D structure (shown in Fig. 4c–d). The KOH penetrates between the layers at a high temperature of 800 °C utilizing chemical activation, producing full separation of layers into thin sheets with the insertion of pores to produce a 3D framework. As a result, CDPC with a wide range of pore ranges is projected to function very well electrochemically. The proportion of carbon, oxygen, and other elemental content in the material has also been investigated using energy dispersive spectroscopy (EDS). The heteroatoms sulphur and oxygen offer additional redox activity throughout the charge-discharge process. Due to the quick electron movement in between the oxygen atoms due to its electronegative character, the presence of oxygen atoms is predicted to give additional electrical conductivity. Fig. 4e show the elemental mapping of the CDPC sample. The three types of elements (carbon, oxygen, and sulphur) were discovered in the CDPC sample, as shown in Fig. 4f by the EDS spectrum. There were no impurity element peaks in the sample. As expected, the sample was primarily made up of carbon components. In the inset of Fig. 4f, the proportion of different elements in the sample is shown. The presence of Sulphur in the sample, estimated to be about 0.8 %, can be attributable to the pre-carbonization treatment of cow dung with sulphuric acid.

### 3.2. Electrochemical studies of CDPC electrodes

We investigated CDPC as a SC electrode after being inspired by its unique properties. The electrochemical parameters of CDPC electrodes are assessed using CV and GCD measurements in 3-electrode system. The CDPC electrode's performance is evaluated using 1 M H<sub>2</sub>SO<sub>4</sub> electrolyte. Previous literature publications were used to determine the molarity of the electrolyte solutions. To begin, the electrode's working potential window was determined by conducting CV at different scan rate in 1 M H<sub>2</sub>SO<sub>4</sub>, as illustrated in Fig. 5a. The CDPC electrode has been scanned wrt open circuit potential (OCP). The potential climbed until the CV curve showed a rapid rise in current, indicating that the electrolyte was decomposing. As a result, the electrode's working potential window has been set between the OCP and the breakdown of the electrolyte's initial potential [32]. The CDPC electrode's maximum functioning potential

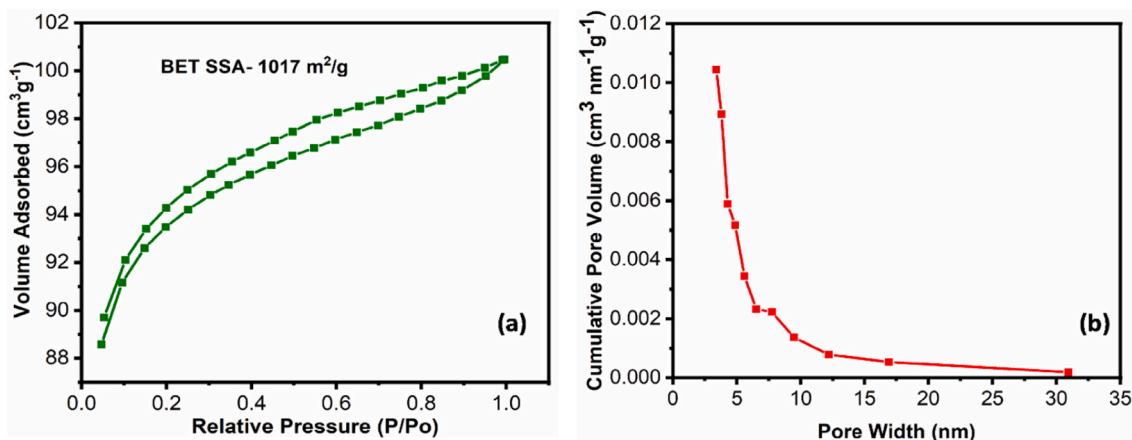
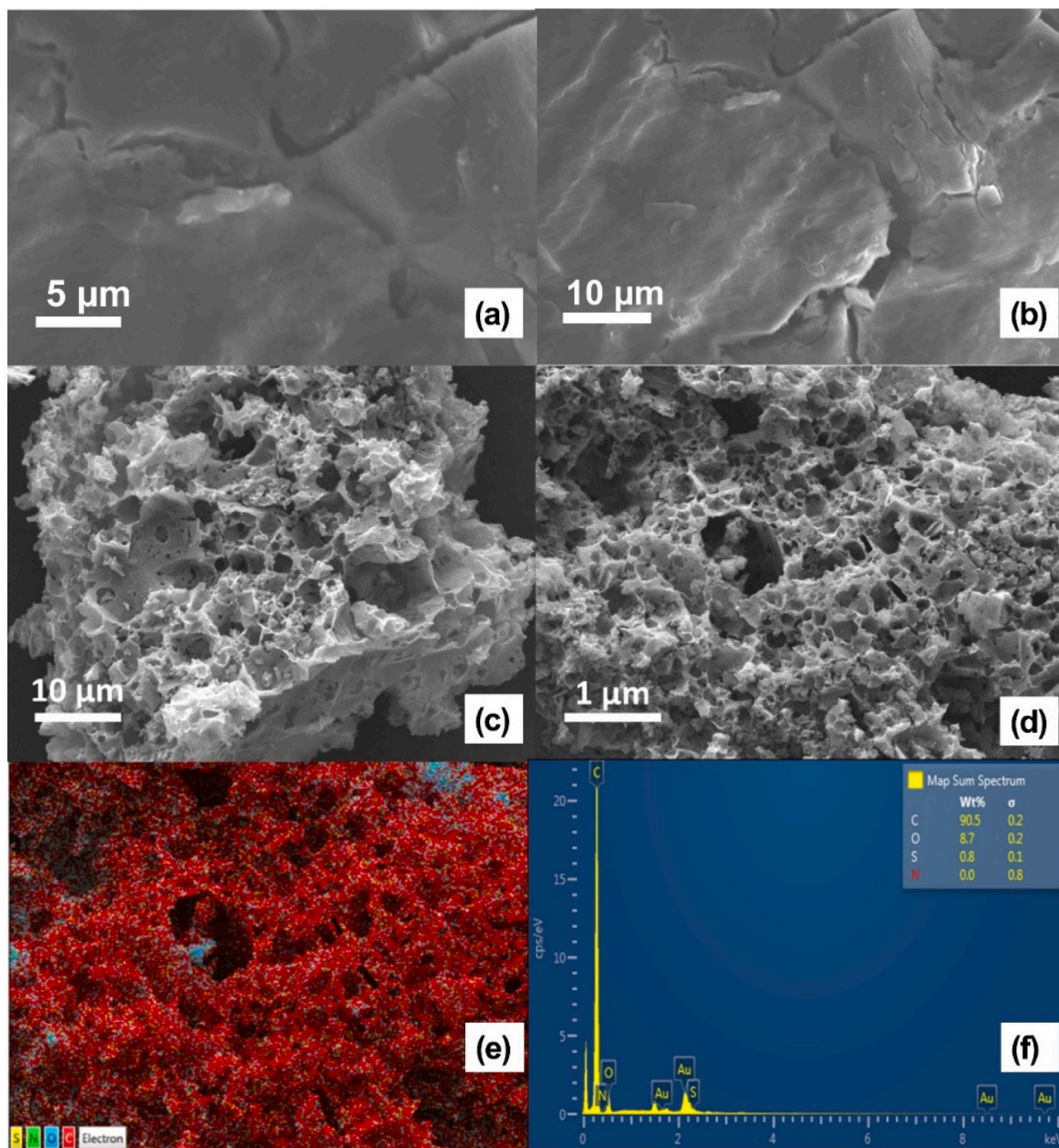


Fig. 3. (a) N<sub>2</sub> adsorption-desorption isotherms, and (b) BJH pore-size of CDPC material.





**Fig. 4.** Morphological and elemental characterization of CDPC sample: (a) & (b) FESEM at different scales of the pre-carbonized carbon, (c) & (d) FESEM at different scales of the carbon (CDPC) after activation of pre-carbonized carbon (c) elemental mapping in CDPC, (d) EDS elemental characterization of CDPC.

window was determined to be 0.0–1.0 V. All of the CV curves of the CDPC electrode display a quasi-rectangular form without any redox peaks when using 1 M  $\text{H}_2\text{SO}_4$  acidic electrolyte, as illustrated in Fig. 5a. This confirms the EDLC character of the CDPC electrode by indicating the production of EDL over the surface of CDPC. This is due to the existence of mesopores in the CDPC sample, which aid the CDPC electrode in maintaining its perfect rectangular behaviour (EDLC feature) even at greater scan speeds. The presence of EDLC exists at higher scan speed validates CDPC electrodes' extremely high power capability (for supercapacitor applications). The CDPC 3D framework's mesoporous structure provides an electrolyte reservoir as well as adequate ionic conducting routes for fast ionic mobility of electrolyte ions. As a result,

the existence of hierarchical pores in CDPC increases this process greatly by giving a larger SSA, which is also helpful for better energy density and long cycle life. Using CV data, the  $C_s$  for CDPC electrode is evaluated using Eq. 1. The highest specific capacitance determined using CV analysis is 178 F/g in 1 M  $\text{H}_2\text{SO}_4$  electrolyte at 5 mV/s.

GCD measurements are used to evaluate the more accurate usefulness of CDPC electrodes in 1 M  $\text{H}_2\text{SO}_4$  electrolyte. Fig. 5b shows the linear charge-discharge behaviour in a nearly perfect rectangular curve. The linear GCD profiles are typical of EDLC, indicating that the CDPC electrodes as manufactured have a high coulombic efficiency. The triangular GCD profiles may also be seen at greater current densities, indicating that CDPC electrodes have a good rate performance.

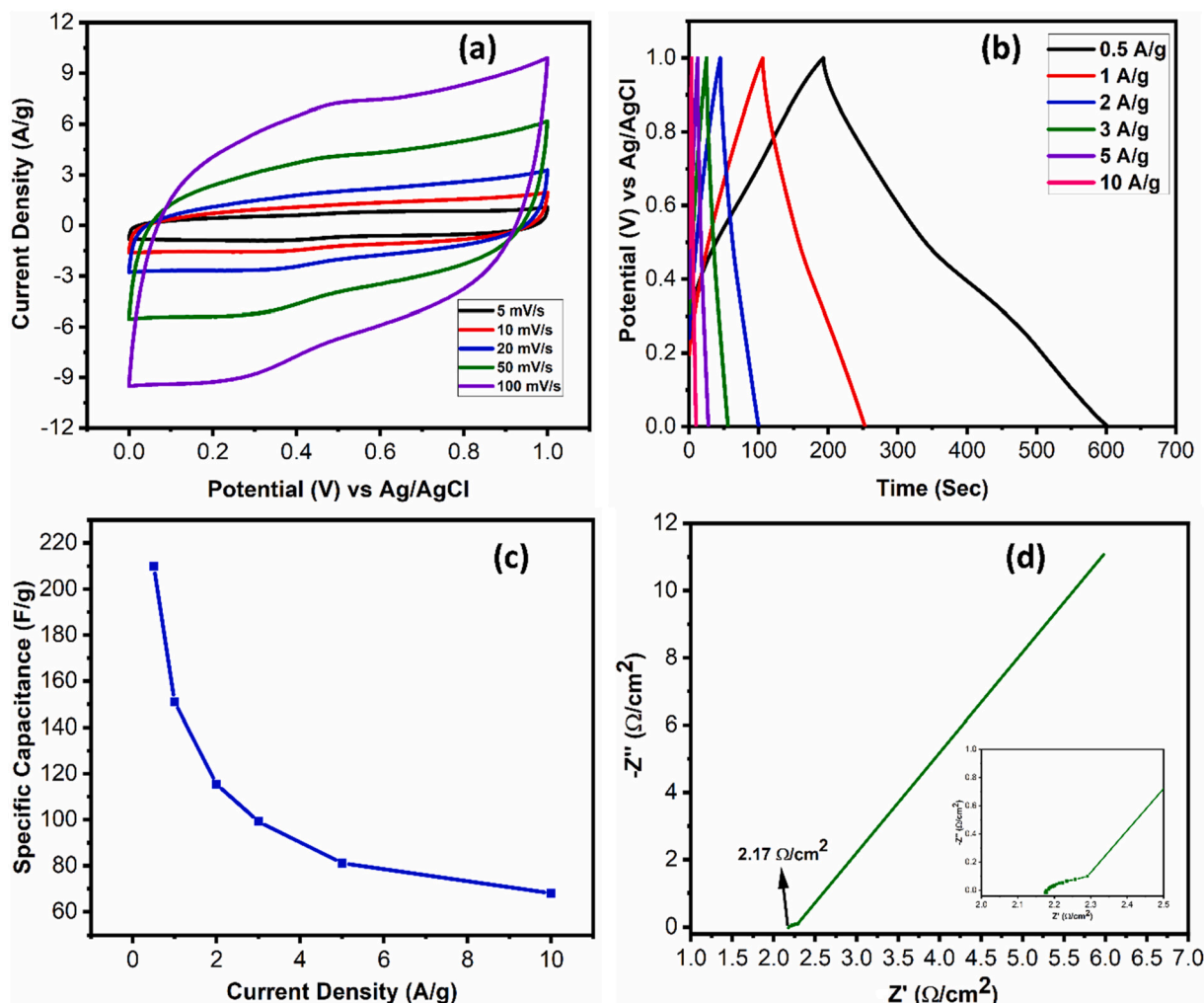


Fig. 5. Electrochemical comparison of CDPC electrode in 1 M H<sub>2</sub>SO<sub>4</sub>: (a) CV at different scan rates, (b) GCD at different constant current density, (c) variation of specific capacitance with current density, and (d) Nyquist plot.

However, a bit non-linearity is observed at low current density which is due to the presence of heteroatoms (O and S) which provide the functional sites and add some pseudocapacitance value to the material [21,33].

The current has a substantial influence on the CDPC charge storage behaviour, according to GCD curves. The CDPC electrode shows the highest Cs of 210 F/g in 1 M H<sub>2</sub>SO<sub>4</sub> electrolyte at 0.5 A/g. Fig. 5c depicts the change in Cs as a function of current density in various electrolyte systems. The characteristics reveal that when the current density increases, the Cs falls due to increasing potential drops. This occurs because of diffusion-limited process, in which the ions does not completely penetrate the interior pores of the electrode at higher current densities. To put it another way, the absence of a smooth inner-pore transport channel causes large losses due to ion diffusion, which lead to a larger potential drop at higher current densities.

The Nyquist plot derived using EIS is shown in Fig. 5d that determines the impedance parameters. The Nyquist plot is divided into two parts: the high-frequency area (where the plot begins) and the low-frequency region (where the plot ends). The  $R_s$  and  $R_{ct}$  may be calculated using the Nyquist plot's high-frequency area. The  $R_s$  is equal to the length of the x-axis from the Nyquist plot's starting point, while the  $R_{ct}$  is equal to the length of the semicircle in the high-frequency zone. The series equivalency resistance was determined to be 2.17 Ω/cm<sup>2</sup> from the enlarged Nyquist plot, whereas the  $R_{ct}$  was calculated to be 0.14 Ω/cm<sup>2</sup> for 1 M H<sub>2</sub>SO<sub>4</sub>. The low resistance results in the high performance of the

CDPC.

The CDPC electrode provided improved specific capacitance values and stability, as evidenced by all CV and GCD experiments. The CDPC electrode's superior supercapacitor performance is owing to the existence of a greater number of reaction sites (C=O, C—O, and O—H, H<sup>+</sup>) provided by the functionalities arising from heteroatoms such as oxygen and sulphur in the material. Beside the natural EDLC behaviour of carbon, these heteroatoms provide pseudocapacitance value to the material by providing these functional sites. As a result, charge contribution studies are required to establish the electrochemical parameters of CDPC electrodes with greater accuracy.

### 3.3. Charge contribution studies for CDPC electrodes

The material's specific capacitance (Cs) is made up of two sorts of processes: (i) surface and (ii) diffusion, both of which have been studied previously. Because their dependency on scan rate ( $v$ ) is entirely distinct, both contributions may be estimated. The current generated by a surface-controlled reaction is proportional to scan rate ( $v$ ). The reliance of the diffusion, on the other hand, varies linearly with  $v^{1/2}$ . The current fluctuates with scan rate as follows, according to the Dunn method when considering the preceding statement [24,34,35]:

For, surface controlled current:

$$I_s = k_1 v \quad (5)$$

For, diffusion controlled current:

$$I_D = k_2 \nu^{1/2} \quad (6)$$

$k_1$  and  $k_2$  are the proportionality constants, while  $I_s$  and  $I_D$  are the surface and diffusion currents, respectively. Both sorts of operations may be seen in the material. As a result, the total current is equal to the sum of surface and diffusion-controlled currents

$$I = I_s + I_D \quad (7)$$

$$\text{Or, } \frac{I}{\nu^{1/2}} = k_1 \nu^{1/2} + k_2 \quad (8)$$

The straight-line Eq. 8, and its slope/intercept may be used to evaluate the surface and diffusion-controlled process contributions. The surface charge contribution was determined and presented in Fig. 6a and b at a scan rate of 5 & 100 mV/s.

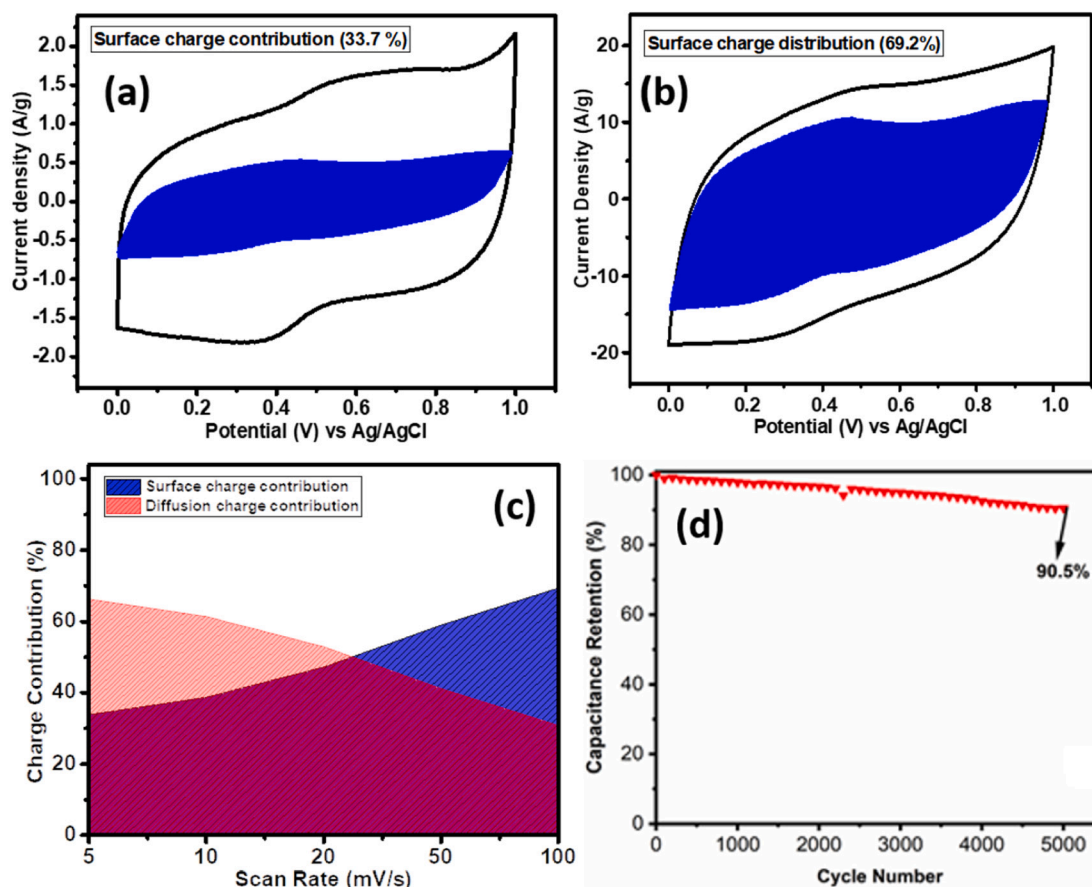
The blue shaded region corresponds to the surface charge contribution region. It is noted that surface charge contribution is more pronounced in higher scan rate than that of low scan rate. Additionally, Fig. 6c also shows the relationship between the proportion of diffusion charge contribution and the scan rate. This shows that diffusion contribution increases with decreasing scan rates. Hence it is observed that surface based charge contribution transformed into diffusion based charge contribution when transiting from high scan rate to low scan rates. Because the cyclic stability test is such an important criterion in determining the practical application of the developed electrode. To test the stability of the CDPC electrode, 5000 cycles were performed (Fig. 6d). In a 1 M  $H_2SO_4$  solution, about 90.5 % of the original capacitance was preserved. This excellent cyclic stability results in high rate

capability of electrode which in turn gives high-performance supercapacitor.

#### 3.4. Study of symmetrical supercapacitor device

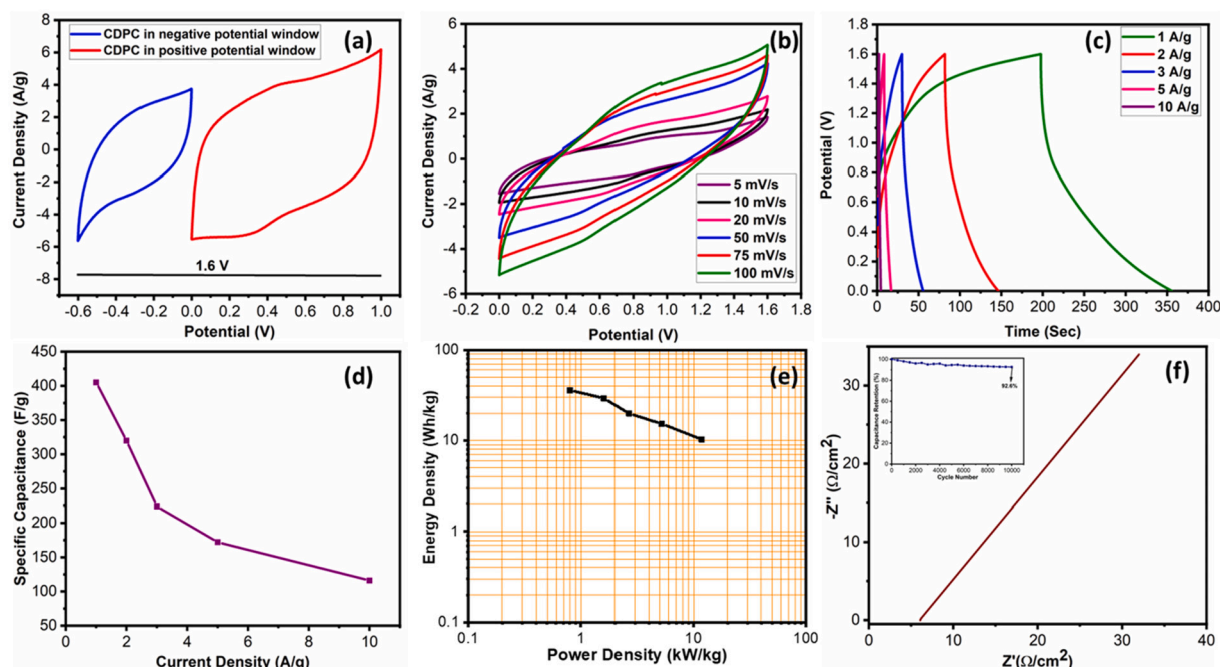
A solid-state symmetrical SC device was also assembled utilizing CDPC electrode owing to its convincing electrochemical performance of CDPC. While using CDPC as a negative electrode, its voltage was optimized by performing CV, which was discovered to climb up to  $-0.6$  V, with the degradation of electrolyte degrades after this range. Fig. 7a shows the single electrode's merged CV in negative and positive potential. As a result of the merged CV of the CDPC electrode in the +ve and -ve windows, the working voltage window for the CDPC//CDPC SC is up to 1.6 V. The CV of an assembled symmetric supercapacitor was also investigated from 5 to 100 mV/s and as illustrated in Fig. 7b, A deviation from rectangular behaviour at lower scan rates is due to the surface reactions that happened with the presence of sulphur & oxygen. It's also worth noting that with increasing scan rate, the current rises slowly, implying that voltammetry current is proportional to scan rate. Because of the mesoporous characteristics of CDPC material, this rise in current and EDLC behaviour is expected. Mesopores of CDPC, on the other hand, promotes rapid ionic transit hence facilitating high performance. Furthermore, even at high current densities, very symmetric GCD curves (as seen in Fig. 7c) suggest ideal capacitive nature of SC.

Fig. 7d shows the variation of specific capacitance with current densities. At 1 A/g, the symmetric device shows the highest specific capacitance of 405 F/g. The as assembled symmetric device also displayed high specific capacitance of 116 F/g (10 A/g). Energy density and power density of SC device is calculated using Eqs. 3 and 4, respectively. The device in PVA-1 M  $H_2SO_4$  polymer gel electrolyte gave the



**Fig. 6.** Surface and diffusion charge contribution study of CDPC: (a) surface charge contribution study at 100 mV/s; (b) surface charge contribution study at 5 mV/s; (c) surface and diffusion charge contribution comparison at different scan rates; and (d) capacitance retention vs cycle number.





**Fig. 7.** Electrochemical performance of CDPC//CDPC symmetrical supercapacitor device: (a) combined CV of CDPC in negative and positive potential window; (b) CV at varying scan rates; (c) GCD at varying current density; (d) variation of specific capacitance with current density; (e) Ragone plot; and (f) capacitance retention variation with number of cycles (inset: Nyquist plot).

maximum energy density of 36 Wh/kg with a matching power density of 800 W/kg (Fig. 7e).

The Nyquist plot is used to compute the equivalent series resistance (ESR) (Fig. 7f inset). The EIS measurements match well with the GCD and CV results, as there is no semi-circular curve in the high-frequency regime, indicating that the device has a very low charge transfer resistance. In addition, the device's ESR was measured at  $6.15 \Omega \cdot \text{cm}^2$ , based on the real axis intercept. In addition, besides energy density, power density, cyclic stability is also a critical parameter to understand the practicality of the device. Fig. 7f depicts the variation of capacitance retention wrt cycle number. Even after 10,000 continuous charge/discharge cycles with 98.9 % coulombic efficiency, the symmetric device maintains long cycle life of 92.6 %. Clearly, the low-cost solid-state symmetric supercapacitor device CDPC//CDPC offers outstanding electrochemical performance. Furthermore, the comparison of the findings of this study with previously published literatures have been tabulated in Table 1.

#### 4. Conclusion

In this study, cow dung is employed as a biowaste resource to create extremely porous and conductive carbon with a 3D structure and linked

pores. The CDPC is employed as a potential electrode for supercapacitors because of its remarkable porosity. When evaluated in a three-electrode setup with 1 M  $\text{H}_2\text{SO}_4$  electrolyte, the CDPC electrode shows superior electrochemical evaluation and rendered Cs of 210 F/g at 0.5 A/g. In addition, CDPC preserved 90.5 % of its initial capacitance value after 5000 GCD cycles. The surface-controlled reaction, which is significantly more enhanced than diffusion-controlled reaction at higher scan rates. Furthermore, the symmetrical solid-state supercapacitor device had a high energy density of 36 Wh/kg and a decent power density of 800 W/kg, as well as outstanding cyclic stability, retaining 92.6 % of original capacitance after 10,000 GCD cycles. These findings demonstrated that charge contribution strategy has a substantial impact on SC electrode performance.

#### CRediT authorship contribution statement

PD has performed the experiments and electrochemical characterizations of various electrodes and also wrote the first draft of manuscript. VS contributed in the calculations and analysis of surface-diffusion parameters. BG has done the structural and morphological analysis of materials. MH performed the XPS of the samples and analysis of the data including fitting and explanation. WN contributed in data

**Table 1**  
Comparison of performance of the present study with previous reported literature.

Sr. no	Material	Electrolyte	Specific capacitance (F/g)	Energy density (Wh/kg)	Power density (kW/kg)	Cyclic stability	Ref
1	Rice straw	1 M $\text{H}_2\text{SO}_4$	332	7.8	0.15	99 (5000)	[36]
2	Corn cob	6 M KOH	293 (1 A/g)	20.15	0.5	99.9 (4000)	[37]
3	Rubber wood	1 M $\text{H}_2\text{SO}_4$	129 (1 mV/s)	14.2	0.5	—	[38]
4	Pomelo peel	—	260 (1 A/g)	27.75	0.3	84.2 (10000)	[39]
5	Banana peel	6 M KOH	210 (0.5 A/g)	—	—	~100 (5000)	[40]
6	Tree bark	6 M KOH	286 (0.5 A/g)	34.6	0.36	70.8 (5000)	[41]
7	Jackfruit shell	0.5 M KOH	292 (1 A/g)	40	1.48	94 (10,000)	[42]
8	Peanut Shell	0.1 M $\text{H}_2\text{SO}_4$	291	—	—	—	[43]
9	Pitaya peel	6 M KOH	255 (1 A/g)	—	—	96.4 (5000)	[44]
10	Dead neem leaves	1 M $\text{H}_2\text{SO}_4$	88 (2 A/g)	56	0.22	92 (2000)	[45]
11	Longan shell	6 M KOH	210 (0.5 A/g)	17.2	1	100 (10000)	[46]
12	Cow dung	1 M $\text{H}_2\text{SO}_4$	210 (0.5 A/g)	36	0.80	92.6 (10000)	This work



interpretation, discussion and edited the first draft of the manuscript. SS conceptualized, supervised and executes the project and corrected & wrote various drafts of the manuscript.

### Declaration of competing interest

The authors declare that they have no known competing financial interests or personal relationships that could have appeared to influence the work reported in this paper.

### Data availability

Data will be made available on request.

### Acknowledgment

PD gratefully acknowledges his research fellowship received from the CSIR, India. SS acknowledges the CSIR for awarding Nehru Science Post-Doctoral Fellowship (HRDG/CSIR-Nehru PDF/EN, ES & PS/EMR-1/02/2019). SS and VS also want to acknowledge funding from the European Union's Horizon 2020 research and innovation programme under the Marie Skłodowska-Curie grant agreement No 847639. B.G. acknowledges funding from the European Union's Horizon 2020 research and innovation programme under the Marie Skłodowska-Curie grant agreement No. 847413. Scientific work is published as part of an international cofinanced project founded from the programme of the Minister of Science and Higher Education entitled "PMW" in the years 2020–2024; agreement no. 5005/H2020-MSCA-COFUND/2019/2.

### References

- [1] P. Simon, Y. Gogotsi, Perspectives for electrochemical capacitors and related devices, *Nat. Mater.* 19 (2020) 1151–1163.
- [2] B.E. Conway, Transition from "Supercapacitor" to "Battery" behavior in electrochemical energy storage, *J. Electrochem. Soc.* 138 (1991) 1539–1548.
- [3] P. Simon, Y. Gogotsi, Materials for electrochemical capacitors in nanoscience and technology: a collection of reviews from Nature journals, World Scientific (2010) 320–329.
- [4] S. Sundriyal, V. Shrivastav, H.D. Pham, S. Mishra, A. Deep, D.P. Dubal, Advances in bio-waste derived activated carbon for supercapacitors: trends, challenges and prospective, *Resour. Conserv. Recycl.* 169 (2021), 105548.
- [5] Z.S. Iro, C. Subramani, S. Dash, A brief review on electrode materials for supercapacitor, *Int. J. Electrochem. Sci.* 11 (2016) 10628–10643.
- [6] F. Béguin, V. Presser, A. Balducci, E.J.A.m. Frackowiak, Supercapacitors: carbons and electrolytes for advanced supercapacitors, *Advanced Materials* 26 (2014) 2283.
- [7] J. Gamby, P. Taberna, P. Simon, J. Fauvarque, M. Chesneau, Studies and characterisations of various activated carbons used for carbon/carbon supercapacitors, *J. Power Sources* 101 (2001) 109–116.
- [8] Z. Song, L. Miao, L. Li, D. Zhu, L. Gan, M. Liu, A robust strategy of solvent choice to synthesize optimal nanostructured carbon for efficient energy storage, *Carbon* 180 (2021) 135–145.
- [9] W. Zhang, B. Liu, M. Yang, Y. Liu, H. Li, P. Liu, Biowaste derived porous carbon sponge for high performance supercapacitors, *J. Mater. Sci. Technol.* 95 (2021) 105–113.
- [10] D. Yu, C. Chen, G. Zhao, L. Sun, B. Du, H. Zhang, Z. Li, Y. Sun, F. Besenbacher, M. Yu, Biowaste-derived hierarchical porous carbon nanosheets for ultrahigh power density supercapacitors, *ChemSusChem* 11 (2018) 1678–1685.
- [11] P. Dubey, V. Shrivastav, P.H. Maheshwari, S. Sundriyal, Recent advances in biomass derived activated carbon electrodes for hybrid electrochemical capacitor applications: challenges and opportunities, *Carbon* 170 (2020) 1–29.
- [12] M. Mansuer, L. Miao, D. Zhu, H. Duan, Y. Lv, L. Li, M. Liu, L. Gan, Facile construction of highly redox active carbons with regular micropores and rod-like morphology towards high-energy supercapacitors, *Mater. Chem. Front.* 5 (2021) 3061–3072.
- [13] S. Sundriyal, V. Shrivastav, A. Gupta, V. Shrivastav, A. Deep, S.R. Dhakate, Pencil peel derived mixed phase activated carbon and metal-organic framework derived cobalt-tungsten oxide for high-performance hybrid supercapacitors, *Mater. Res. Bull.* 142 (2021), 111396.
- [14] S. Saha, D. Potphode, C.S. Sharma, Borassus flabellifer fruit flesh derived hierarchical porous partly graphitic carbon as a sustainable electrode for supercapacitors, *Energy Fuel* 36 (2021) 638–654.
- [15] D. Chen, L. Yang, J. Li, Q. Wu, Effect of self-doped heteroatoms in biomass-derived activated carbon for supercapacitor applications, *ChemistrySelect* 4 (2019) 1586–1595.
- [16] J. Han, Q. Li, J. Wang, J. Ye, G. Fu, L. Zhai, Y. Zhu, Heteroatoms (O, N)-doped porous carbon derived from bamboo shoots shells for high performance supercapacitors, *J. Mater. Sci. Mater. Electron.* 29 (2018) 20991–21001.
- [17] M. Karuppannan, Y. Kim, Y.E. Sung, O.J. Kwon, Nitrogen and sulfur co-doped graphene-like carbon sheets derived from coir pith bio-waste for symmetric supercapacitor applications, *J. Appl. Electrochem.* 49 (2019) 57–66.
- [18] L. Lyu, K.D. Seong, D. Ko, J. Choi, C. Lee, T. Hwang, Y. Cho, X. Jin, W. Zhang, H. Pang, Y. Piao, Recent development of biomass-derived carbons and composites as electrode materials for supercapacitors, *Mater. Chem. Front.* 3 (2019) 2543–2570.
- [19] D. Xue, D. Zhu, W. Xiong, T. Cao, Z. Wang, Y. Lv, L. Li, M. Liu, L. Gan, Template-free, self-doped approach to porous carbon spheres with high N/O contents for high-performance supercapacitors, *ACS Sustain. Chem. Eng.* 7 (2019) 7024–7034.
- [20] Z. Song, L. Miao, H. Duan, L. Ruhlmann, Y. Lv, D. Zhu, L. Li, L. Gan, M. Liu, Anionic co-insertion charge storage in dinitrobenzene cathodes for high-performance aqueous zinc-organic batteries, *Angew. Chem. Int. Ed.* 134 (2022), e202208821.
- [21] A. Gopalakrishnan, A. Yu, S. Badhulika, Facile synthesis of highly porous N-doped carbon nanosheets with silica nanoparticles for ultrahigh capacitance supercapacitors, *Energy Fuel* 34 (2020) 11508–11518.
- [22] A. Gopalakrishnan, S. Badhulika, From onion skin waste to multi-heteroatom self-doped highly wrinkled porous carbon nanosheets for high-performance supercapacitor device, *J. Energy Storage* 38 (2021), 102533.
- [23] P. Dubey, V. Shrivastav, M. Singh, P.H. Maheshwari, S. Sundriyal, S.R. Dhakate, Electrolytic study of pineapple Peel derived porous carbon for all-solid-state supercapacitors, *Chem. Select* 6 (2021) 11736–11746.
- [24] P. Dubey, V. Shrivastav, A. Kaur, P.H. Maheshwari, S. Sundriyal, Surface and diffusion charge contribution studies of human hair-derived heteroatom-doped porous carbon electrodes for supercapacitors, *Energy Fuel* 36 (2021) 626–637.
- [25] S. Sundriyal, V. Shrivastav, A. Kaur, P. Dubey, S. Mishra, A. Deep, S.R. Dhakate, Waste office papers as a cellulosic material reservoir to derive highly porous activated carbon for solid-state electrochemical capacitor, *IEEE Trans. Nanotechnol.* 20 (2021) 481–488.
- [26] S. Sundriyal, V. Shrivastav, P. Dubey, M. Singh, A. Deep, S.R. Dhakate, Highly porous carbon from azadirachta indica leaves and UIO-66 derived metal oxide for asymmetrical supercapacitors, *IEEE Trans. Nanotechnol.* 21 (2022) 60–65.
- [27] W. Tian, Q. Gao, Y. Tan, K. Yang, L. Zhu, C. Yang, H. Zhang, Bio-inspired beehive-like hierarchical nanoporous carbon derived from bamboo-based industrial by-product as a high performance supercapacitor electrode material, *J. Mater. Chem. A* 3 (2015) 5656–5664.
- [28] A. Adan-Mas, L. Alcaraz, P. Arévalo-Cid, F.A. López-Gómez, F. Montemor, Coffee-derived activated carbon from second biowaste for supercapacitor applications, *Waste Manag.* 120 (2021) 280–289.
- [29] Y. Qin, L. Miao, M. Mansuer, C. Hu, Y. Lv, L. Gan, M. Liu, Spatial confinement strategy for micelle-size-mediated modulation of mesopores in hierarchical porous carbon nanosheets with an efficient capacitive response, *ACS Appl. Mater. Interfaces* 14 (2022) 33328–33339.
- [30] A. Gopalakrishnan, S. Badhulika, Gelatinization assisted synthesis of multi-heteroatoms enriched 3D honeycomb-like porous carbon for high-voltage supercapacitor device, *J. Energy Storage* 43 (2021), 103261.
- [31] Z. Song, H. Duan, L. Miao, L. Ruhlmann, Y. Lv, W. Xiong, D. Zhu, L. Li, L. Gan, M. Liu, Carbon hydrangeas with typical ionic liquid matched pores for advanced supercapacitors, *Carbon* 168 (2020) 499–507.
- [32] L. Miao, H. Duan, Z. Wang, Y. Lv, W. Xiong, D. Zhu, L. Gan, L. Li, M. Liu, Improving the pore-size compatibility between poly (ionic liquid)-derived carbons and high-voltage electrolytes for high energy-power supercapacitors, *Chem. Eng. J.* 382 (2020), 122945.
- [33] L. Miao, H. Duan, D. Zhu, Y. Lv, L. Gan, L. Li, M. Liu, Boron "gluing" nitrogen heteroatoms in a prepolymerized ionic liquid-based carbon scaffold for durable supercapacitive activity, *J. Mater. Chem. A* 9 (2021) 2714–2724.
- [34] J. Wang, J. Polleux, J. Lim, B. Dunn, Pseudocapacitive contributions to electrochemical energy storage in TiO<sub>2</sub> (anatase) nanoparticles, *J. Phys. Chem. A* 111 (2007) 14925–14931.
- [35] S. Sundriyal, V. Shrivastav, A. Kaur, A. Deep, S.R. Dhakate, Surface and diffusion charge contribution study of neem leaves derived porous carbon electrode for supercapacitor applications using acidic, basic, and neutral electrolytes, *J. Energy Storage* 41 (2021), 103000.
- [36] N. Sudhan, K. Subramani, M. Karnan, N. Ilayaraja, M. Sathish, Biomass-derived activated porous Carbon from Rice straw for a high-energy symmetric supercapacitor in aqueous and non-aqueous electrolytes, *Energy Fuel* 31 (2016) 977–985.
- [37] S. Yang, K. Zhang, Converting corn cob to activated porous carbon for supercapacitor application, *Nanomaterials* 8 (2018) 181.
- [38] U. Thubsuang, S. Laebang, N. Manmuanpom, S. Wongkasemjit, T. Chaisuwan, Tuning pore characteristics of porous carbon monoliths prepared from rubber wood waste treated with H<sub>3</sub>PO<sub>4</sub> or NaOH and their potential as supercapacitor electrode materials, *J. Mater. Sci.* 52 (2017) 6837–6855.
- [39] G. Qu, S. Jia, H. Wang, F. Cao, L. Li, C. Qing, D. Sun, B. Wang, Y. Tang, J. Wang, Asymmetric supercapacitor based on porous N-doped carbon derived from pomelo peel and NiO arrays, *ACS Appl. Mater. Interfaces* 8 (2016) 20822–20830.
- [40] B. Liu, L. Zhang, P. Qi, M. Zhu, G. Wang, Y. Ma, X. Guo, H. Chen, B. Zhang, Z. Zhao, Nitrogen-doped banana peel-derived porous carbon foam as binder-free electrode for supercapacitors, *Nanomaterials* 6 (2016) 18.
- [41] F. Yu, Z. Ye, W. Chen, Q. Wang, H. Wang, H. Zhang, C. Peng, Plane tree bark-derived mesopore-dominant hierarchical carbon for high-voltage supercapacitors, *Appl. Surf. Sci.* 507 (2020), 145190.

- [42] K. Lee, L. Shabnam, S.N. Faisal, V.G. Gomes, Aerogel from fruit biowaste produces ultracapacitors with high energy density and stability, *J. Energy Storage* 27 (2020), 101152.
- [43] D. Kalpana, Y.S. Lee, Effects of temperature and pore structure on high surface area-activated carbon obtained from Peanut shells, *J. Nanosci. Nanotechnol.* 16 (2016) 2950–2955.
- [44] W. Lu, X. Cao, L. Hao, Y. Zhou, Y. Wang, Activated carbon derived from pitaya peel for supercapacitor applications with high capacitance performance, *Mater. Lett.* 264 (2020), 127339.
- [45] M. Biswal, A. Banerjee, M. Deo, S. Ogale, From dead leaves to high energy density supercapacitors, *Energy Environ. Sci.* 6 (2013) 1249–1259.
- [46] J. Yan, Y.Y. Fang, S.W. Wang, S.D. Wu, L.X. Wang, Y. Zhang, H.W. Luo, Y. Cao, H. L. Gao, L.Z. Wang, Nitrogen-doped oxygen-rich activated carbon derived from longan Shell for supercapacitors, *Int. J. Electrochem. Sci.* 15 (2020) 20964.